Nanoscale
Advances

ROYAL SOCIETY
OF CHEMISTRY

PAPER

View Article Online
View Journal | View Issue

Check for updates

Cite this: *Nanoscale Adv.*, 2023, **5**, 5102

A Cu@ZIF-8 encapsulated antibacterial and angiogenic microneedle array for promoting wound healing†

Jieyu Xiang,‡[a] Yufan Zhu,‡[b] Yuanlong Xie,[b] Hang Chen,[a] Ling Zhou,[a] Danyang Chen,[a] Jia Guo,[a] Min Wang,*[a] Lin Cai*[b] and Liang Guo *[a]

Skin wounds caused by external injuries remain a serious challenge in clinical practice. Wound dressings that are antibacterial, pro-angiogenic, and have potent regeneration capacities are highly desirable for wound healing. In this study, a minimally invasive and wound-friendly Cu@ZIF-8 encapsulated PEGDA/CMCS microneedle (MN) array was fabricated using the molding method to promote wound healing. The MNs had good biocompatibility, excellent mechanical strength, as well as strong antibacterial properties and pro-angiogenic effects. When incubated with H_2O_2, Cu@ZIF-8 nanoparticles generated reactive oxygen species, which contributed to their antibacterial properties. Due to the oxidative stress of the cupric ions released from Cu@ZIF-8 and the anti-bacterial capability of the PEGDA/CMCS hydrogel scaffold, such an MN array presents excellent antibacterial activity. Moreover, with the continuous release of Cu ions from the scaffold, such MNs are effective in terms of promoting angiogenesis. With considerable biocompatibility and a minimally invasive approach, the degradable MN array composed of PEGDA/CMCS possessed superior capabilities to continuously and steadily release the loaded ingredients and avoid secondary damage to the wound. Benefiting from these features, the Cu@ZIF-8 encapsulated degradable MN array can dramatically accelerate epithelial regeneration and neovascularization. These results indicated that the combination of Cu@ZIF-8 and degradable MN arrays is valuable in promoting wound healing, which opened a new window for treatment of skin defection.

Received 2nd May 2023
Accepted 12th August 2023

DOI: 10.1039/d3na00291h

rsc.li/nanoscale-advances

1 Introduction

There has been a remarkable focus on wound healing recently because of its severe challenges and serious economic burdens. To solve this, various strategies have been developed, such as hydrogel films, electrospun dressings, and all types of wound patches. Among them, microneedles (MN) are a promising medical technique with the capability of painless transdermal drug delivery *via* a minimally invasive approach, which are widely employed in vaccinations, cancer therapy, dermatological treatments, and cosmetic procedures.[1–5] In particular, the roles of MNs loaded with active ingredients have been studied for accelerating wound healing and therapeutic effects have been observed owing to the increased contact area between the MN patch and the wound.[6–8] However, for some MNs fabricated with non-biodegradable materials, such as stainless steel, the needle body of the MNs easily forms tiny pinholes at the wound sites. There is a high chance that these voids may cause secondary physical damage and even microbial infections in wounds. These drawbacks have severely limited the development of MNs in the field of promotion of wound healing.[9–14] Thus, new-type MN arrays with diverse compositions and expected functions are used in clinical practice.[15–19]

PEGDA hydrogels are hydrophilic polymeric networks with good biocompatibility that are widely used in the field of tissue engineering.[20,21] At the same time, PEGDA can be photo-crosslinked with a photoinitiator under UV light.[22] The plasticity of the whole solution makes it very convenient for MN preparation. In addition, carboxymethyl chitosan (CMCS) is a modified derivative of chitosan, which has good water solubility, strong antibacterial properties and good degradation ability.[23] It is widely used in the biomedical field and has enormous application prospects. But the mechanical strength of CMCS microneedles is not suitable for puncture therapy. We evaluated the impact of the PEGDA and CMCS content on the properties of hydrogels to determine the optimal mechanical strength and degradation ability of hydrogels for MN preparation. The combination of PEGDA/CMCS provides the MN with remarkable mechanical strength, antibacterial effects, and

---

[a] *Department of Plastic Surgery, Zhongnan Hospital of Wuhan University, Wuhan 430071, China. E-mail: wangminwhzn@163.com; orthopedics@whu.edu.cn; guolianghbwh@163.com*

[b] *Department of Spine Surgery and Musculoskeletal Tumor, Zhongnan Hospital of Wuhan University, Wuhan 430071, China*

† Electronic supplementary information (ESI) available. See DOI: https://doi.org/10.1039/d3na00291h

‡ Authors contributed equally.

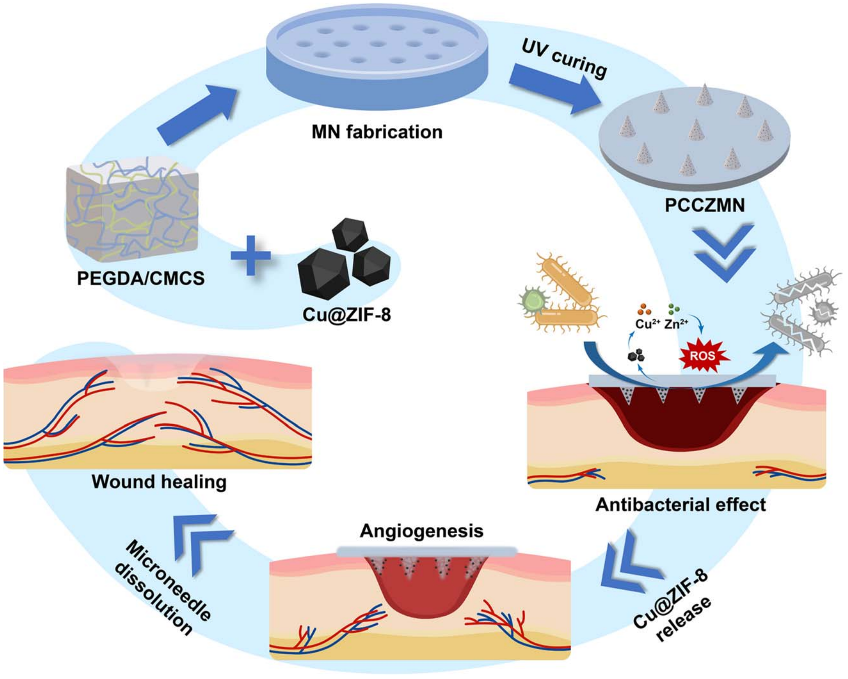

Scheme 1 Schematic illustration of the fabrication and application of MNs, which were fabricated from PEGDA/CMCS and encapsulated with Cu@ZIF-8 nanoparticles *via* a template infusion method.

continuous and steady release of active agents into the wound area.

Copper has been demonstrated to have effective antibacterial properties and pro-angiogenic effects in wound healing.[24–26] Zinc ions are also known to contribute to antibacterial properties and wound healing.[27–29] Recently, copper- and zinc-based zeolitic-imidazolate frameworks (Cu@ZIF-8) have been reported to have an excellent antibacterial effect on the bone repair model.[30] Their nanoparticles generated more reactive oxygen species than ZIF-8, which contributed to their powerful antibacterial properties. The rough surface of the Cu@ZIF-8 nanoparticles can increase the contact area between the MOFs and bacteria, resulting in better antimicrobial activity.[31,32] Furthermore, copper ions play an important role in the vascularization process and can stimulate vascular endothelial cells to form blood vessels.[25,33,34] Thus, Cu@ZIF-8 nanoparticles were selected to modify the properties of PEGDA/CMCS MNs.

In this study, we propose a novel Cu@ZIF-8 encapsulated MN array with features of great biocompatibility, obvious antibacterial activity, and an excellent pro-angiogenic effect. We evaluated the impact of the PEGDA and CMCS content on the properties of hydrogels to determine the optimal mechanical strength and degradation ability of hydrogels for MN preparation. With considerable biocompatibility and a minimally invasive approach, the degradable MN array composed of PEGDA/CMCS possessed superior capabilities to continuously and steadily release the loaded ingredients and avoid secondary damage to the wound. Meanwhile, due to the oxidative stress of the cupric ions released from Cu@ZIF-8 and the anti-bacterial capability of the PEGDA/CMCS hydrogel scaffold, such an MN array presents excellent antibacterial activity. Moreover, with the continuous release of Cu ions from the scaffold, such MNs are effective in terms of promoting angiogenesis.

In conclusion, a minimally invasive and wound-friendly Cu@ZIF-8 encapsulated PEGDA/CMCS microneedle (MN) array was fabricated using the molding method to promote wound healing. The MNs had good biocompatibility, excellent mechanical strength, as well as strong antibacterial properties and pro-angiogenic effects, so we hypothesized that combining PEGDA/CMCS and Cu@ZIF-8 nanoparticles in MNs would be advantageous in promoting wound healing, offering a promising approach for wound healing and other clinical applications (Scheme 1).

2 Materials and methods

2.1. Materials, cell lines, and animals

$Zn(NO_3)_2$ and $Cu(NO_3)_2$ were obtained from MACKLIN. PEGDA, CMCS, and 2-hydroxy-2-methylpropiphenone (HMPP) were purchased from Sigma Aldrich. The ROS detection kit was supplied by the Nanjing Jiancheng Bioengineering Institute. The cells (HUVEC, L929 and RAW264.6) were obtained from the laboratory and were maintained in Dulbecco's modified Eagle medium (Gibco, USA) containing 10% fetal bovine serum (FBS, Gibco, USA) at 37 °C and under 5% CO_2 conditions to cultivate. Male Sprague-Dawley rats, aged 6–8 weeks, were provided by Beijing Vital River Laboratory Animal Technology Co., Ltd. The recommendations in the "Guidelines for the Care and Use of Laboratory Animals in China" to handle animals were strictly followed. All animal procedures were approved by the Experimental Animal Welfare Ethics Committee of the Zhongnan Hospital of Wuhan University.

2.2. Characterization

The surface morphology of the Cu@ZIF-8 nanoparticles and the microstructures of the Cu@ZIF-8@PEGDA/CMCS-MNs were characterized by SEM (VEGA 3 LMU; TESCAN, Czech Republic) with gold sputter coating. X-ray photoelectron spectroscopy (XPS) spectra were obtained using a Thermo Fisher Scientific (ESCALAB250Xi). The element composition of microparticles and MNs was investigated by energy-dispersive spectroscopy (JXA-8530F Plus). X-ray diffraction (XRD) data were collected using an X-ray diffractometer (XPert Pro, PANalytical B.V.).

2.3. Fabrication of the MNs

Cu@ZIF-8 was synthesized according to a previously reported method.[35] Briefly, 1.8 mmol of $Cu\ (NO_3)_2 \cdot 3H_2O$ and 2.2 mmol of $Zn\ (NO_3)_2 \cdot 6H_2O$ were dissolved in 40 ml methanol (Solution A). Solution A was added dropwise to solution B containing 32 mmol 2-methylimidazole and 40 mL methanol using a pump at a speed of 2 mL min^{-1}. Cu@ZIF-8 was collected *via* centrifugation (5000 rpm) after 1 h of reaction at room temperature and washed with methanol 3 times. The powder samples were obtained by drying in a vacuum oven at 50 °C.

CMCS, PEGDA, HMPP (1% v/w), and Cu@ZIF-8 nanoparticles were mixed into the solution. The mixed prepolymer (500 μL) was loaded into a negative mold and placed in a horizontal centrifuge (4000 rpm, 5 min) to infill the MN pinholes. The mixture was then placed on ice and cured under UV irradiation (365 nm, 100 W) for 30 s. Finally, the shaped Cu@ZIF-8@PEGDA/CMCS-MNs were separated from the negative mold.

2.4. Degradation properties of MNs

Different ratios of PEGDA/CMCS-MNs were weighed (W_0), and then immersed in the PBS buffer solution and placed in a shaker (150 rpm, 37 °C). Then, the PBS solution was discarded, and the MNs were fully dried in an oven at 75 °C for 4 h. The residual dry weight of PEGDA/CMCS-MNs was constantly measured during the experiment (W_x). The dry weight ratio (ΔW, %) was calculated using the following equation:

$$\Delta W = \frac{W_0 - W_x}{W_0} \times 100\%$$

2.5. Mechanical strength tests

MNs fabricated with different PEGDA/CMCS ratios were placed on the horizontal specimen stage of an electronic tension testing machine (Instron 5944) with needle tips facing upward. The sensor approached the MNs at a speed of 2 mm min^{-1}. The compression force measurement started when the sensor came into contact with the needle tips and ended when the sensor reached the maximum measuring range of 90 N. Young's modulus was used as the measurement index of the PEGDA/CMCS-MNs. Images of the skin after microneedle penetration were captured using an iPhone 11. Bright-field microscopy was used to detect the insertion depth of the needle tips in the excised rat subcutaneous adipose tissue.

2.6. ROS generation detection

The hydroxylamine colorimetry method was used to determine the ROS concentration in the supernatant. First, 1.5 mg ml^{-1} concentration of Cu@ZIF-8 or ZIF-8 suspensions was incubated in a shaker for 24 h (37 °C, 120 rpm), respectively. The supernatant was then extracted by centrifugation (6000 rpm, 10 min), and the concentration of ROS was detected using an ROS detection kit.

2.7. Antibacterial ability test

S. aureus and *E. coli* were used to evaluate the antimicrobial ability of MNs. MNs with different concentrations of Cu@ZIF-8 (0, 0.5, 1.5, and 2.5 mg mL^{-1}) were immersed in PBS solution, mixed with 100 μL of bacterial solution (1.5 OD value), and incubated at 37 °C for 24 h. 100 μL of the bacterial suspension was dripped onto a culture dish with a solid medium and cultured in a 37 °C incubator for 24 h to form colonies. The bacterial colonies were photographed using an iPhone 11, their numbers were estimated using ImageJ, and the lethality percentage was calculated.

2.8. Ion release curve of the PCCZMNs

The ion release test was performed using a spectrophotometric method. To monitor the Cu^{2+} and Zn^{2+} released from the Cu@ZIF-8@PEGDA/CMCS-MNs, MNs were soaked in 2 mL PBS at 37 °C and then the copper colorimetric assay kit (Beijing League Biotechnology Co., Ltd.) and the zinc colorimetric assay kit (Elabscience Biotechnology Co., Ltd) were used to detect ion release. The obtained standard curve was then used to calculate the cumulative release quantities of Cu^{2+} and Zn^{2+}.

2.9. Cytotoxicity test

The cytotoxicity of MNs was tested using the CCK-8 assay. MNs were immersed in PBS for 24 h (37 °C). Before testing, cells were seeded in 96-well plates and incubated for 24 h to allow them to adhere to the plates. Then, 100 μL of the filtrate of MNs with different Cu@ZIF-8 concentrations (0, 0.5, 1.5, and 2.5 mg mL^{-1}) was used to replace the original medium. The CCK-8 test was conducted on the 1st, 2nd, and 3rd day of incubation.

2.10. Endothelial tube formation assay

For the HUVEC tube formation assay, 1×10^5 HUVECs were seeded onto Matrigel films in 24-well plates and treated with 50% filtrate of MNs (PCMNs and PCCZMNs) and 50% ECM supplemented with 2% FBS. The cells were incubated for 6 h and imaged using bright-field microscopy. The tube length was quantified using Angio Tool software.

2.11. Migration assay

The chemotactic effects of MNs on HUVEC migration were determined using an *in vitro* wound-healing migration assay. Briefly, HUVECs cultured with different media, which included a half fresh complete medium and half filtrate of MNs (PCMNs and PCCZMNs), were seeded in 6-well culture plates at 1×10^5

cells per well and cultured until they reached approximately 90% confluence. The cell monolayer was scratched with a sterile pipette tip to form a wound. HUVECs cultured in a normal medium were used as controls. After incubation for 24 h, the samples were observed using bright-field microscopy. Cell motility was quantified by observing the width of the gap in the wound.

2.12. Rat model establishment and treatment

A rat model of wound healing was established to evaluate and compare the wound healing efficiency of MN treatments. Briefly, 12 male Sprague-Dawley rats (180–220 g) were used for wound induction. Animals were anesthetized by forced 5% isoflurane inhalation, their dorsal fur was shaved, and the target areas were sterilized with povidone-iodine. Two round excisional skin wounds of 10 mm full thickness were created on each side of the midline using a biopsy punch. A donut-shaped silicone splint was glued to the skin with biomedical glue, and the wound was centered on the splint. The latter stabilizes the wound and prevents it from contracting. The rats were randomly assigned to three treatment groups: the control group, pure PEGDA/CMCS-MN (PCMN) group, and Cu@ZIF-8@PEGDA/CMCS-MN (PCCZMN) group. To maximize the function of the MNs, rat backs were covered with breathable plastic films to prevent the wound site from being ground by the rats. Experimental rats were housed in cages with adequate food and water. On the 4th, 8th, and 16th days, wounds were observed and photographed. On the 8th and the 16th day, the rats were euthanized and their subcutaneous regenerated tissues were excised and examined. Body temperature of each group was recorded using an ear thermometer.

2.13. Histology and immunohistochemistry

Neonatal epithelial tissue samples were fixed in 4% (w/v) paraformaldehyde, dehydrated, and embedded in paraffin. Each sample was cut into 7 μm thick slices. All samples were subjected to H&E, Masson's trichrome (Sigma-Aldrich Corp., St. Louis, MO, USA), and CD31 and CD206 immunostaining. The samples were visualized under an inverted and upright fluorescence microscope. New blood vessels were enumerated using ImageJ software (NIH).

2.14. Analysis

Data analysis was conducted using the GraphPad Prism 8 software (GraphPad Software, San Diego, CA, USA). In each group, at least three technical replicates were set up, and the results are presented as the mean ± standard deviation (SD). Differences between two and multiple groups were analyzed by Student's *t*-test and one-way analysis of variance (ANOVA), respectively. In all charts with SD, significant differences are presented by $*P < 0.05$, $**P < 0.01$, $***P < 0.001$, $****P < 0.0001$, and ns: not significant.

3 Results and discussion

3.1. Cu@ZIF-8 nanoparticle characterization

The morphology of the Cu@ZIF-8 nanoparticles was observed by SEM. The images revealed that the Cu@ZIF-8

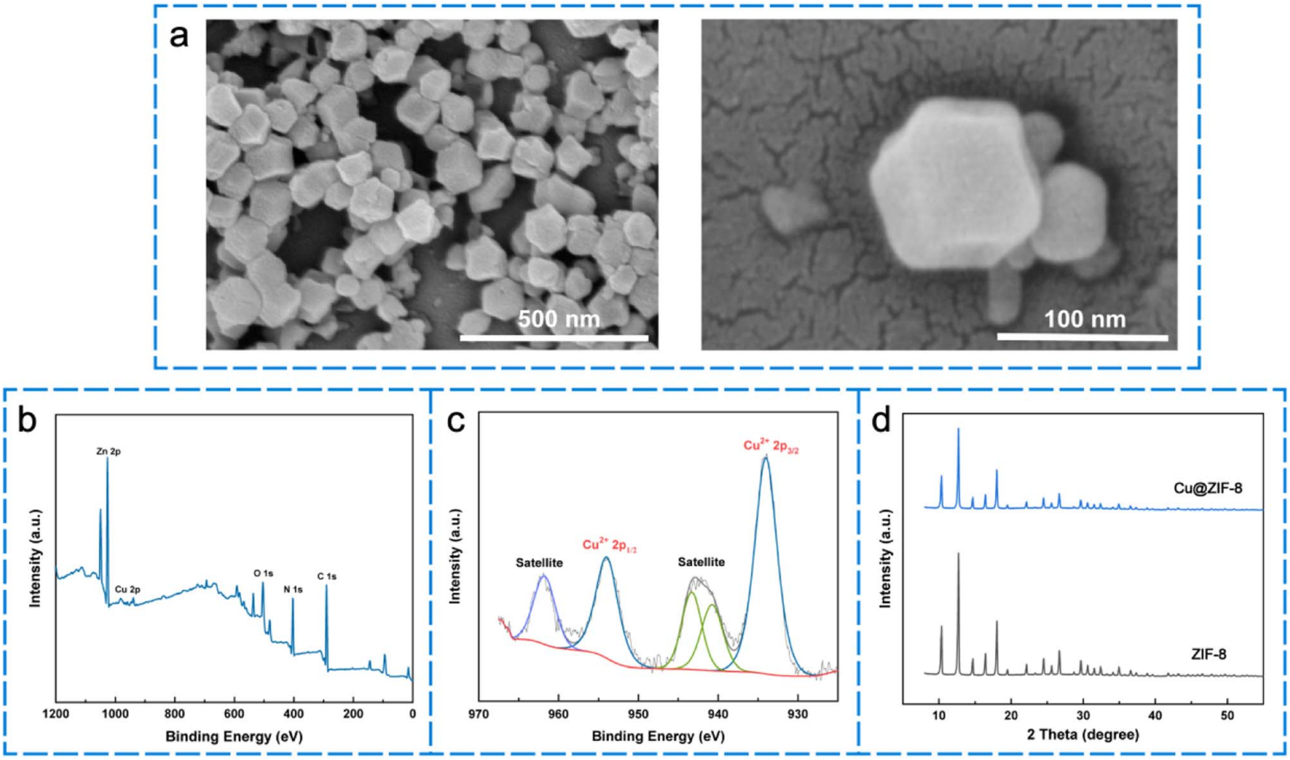

Fig. 1 Characterization of Cu@ZIF-8. (a) SEM image of Cu@ZIF-8. (b and c) XPS spectra of Cu@ZIF-8 in various binding-energy ranges. (d) X-ray diffraction (XRD) spectra of Cu@ZIF-8 and ZIF-8; scale bars are 500 nm and 100 nm in (a), respectively.

nanoparticles had a similar shape (Fig. 1a), with an average diameter of approximately 100 ± 9.67 nm (Fig. 1a). X-ray photoelectron spectroscopy (XPS) indicated that Cu@ZIF-8 was composed of Cu, Zn, C, N, and O (Fig. 1b). As shown in Fig. S1†, the existence of Cu, Zn, C, N and O elements in the resultant Cu@ZIF-8 microparticles was further verified based on the evidence of energy-dispersive X-ray spectroscopy (EDS). All these results revealed the elemental species and distribution in Cu@Zif-8 microparticles and confirmed the successful preparation of Cu@ZIF-8 nanoparticles for the subsequent experiments. Fig. 1c shows the high-resolution XPS spectrum of Cu 2p at 934.01 eV and 953.94 eV corresponding to Cu 2p3/2 and Cu 2p1/2, indicating the successful synthesis of Cu@ZIF-8 NPs. Moreover, the valence state of Cu was proven to be +2 according to the satellite peak between the binding energies of Cu 2p1/2 and Cu 2p3/2.[36–38] The successful synthesis of Cu@ZIF-8 was further validated by powder X-ray diffraction (XRD) characterization (Fig. 1d), which was consistent with the results reported in previous literature and indicates that the doped Cu^{2+} did not cause any structural alteration.[38]

3.2. Characterization of MNs

In this study, biocompatible and biodegradable PEGDA/CMCS mix-hydrogels were selected to manufacture MNs using the molding method. Briefly, the mix-hydrogel was poured and cured on positive molds to obtain a negative mold, which consisted of an orderly array of conical grooves. Then, a two-step molding method was implemented to fabricate the hydrogel MNs (Fig. 2a). In this process, Cu@ZIF-8 nanoparticles were dispersed and mixed with PEGDA/CMCS as the pouring material, and the needle tips were then filled by low-speed centrifugation. After removing the redundant blending, a PEGDA/CMCS mix-hydrogel was added to cover the needle bottoms as a substrate material, after which hydrogel MNs with a certain Young's modulus were obtained by ultraviolet (UV) crosslinking with 2-hydroxy-2-methylpropiophenone (HMPP).

To verify the mechanical strength and biodegradability of the fabricated MNs, we designed and manufactured PEGDA/CMCS-MNs with different mixing ratios, leading to significant differences in the morphology and characteristics of the MNs (Fig. 2b). The SEM images showed that PEGDA/CMCS ratios of 6 : 4 and 4 : 6 were unsuitable for fabricating MNs because of the

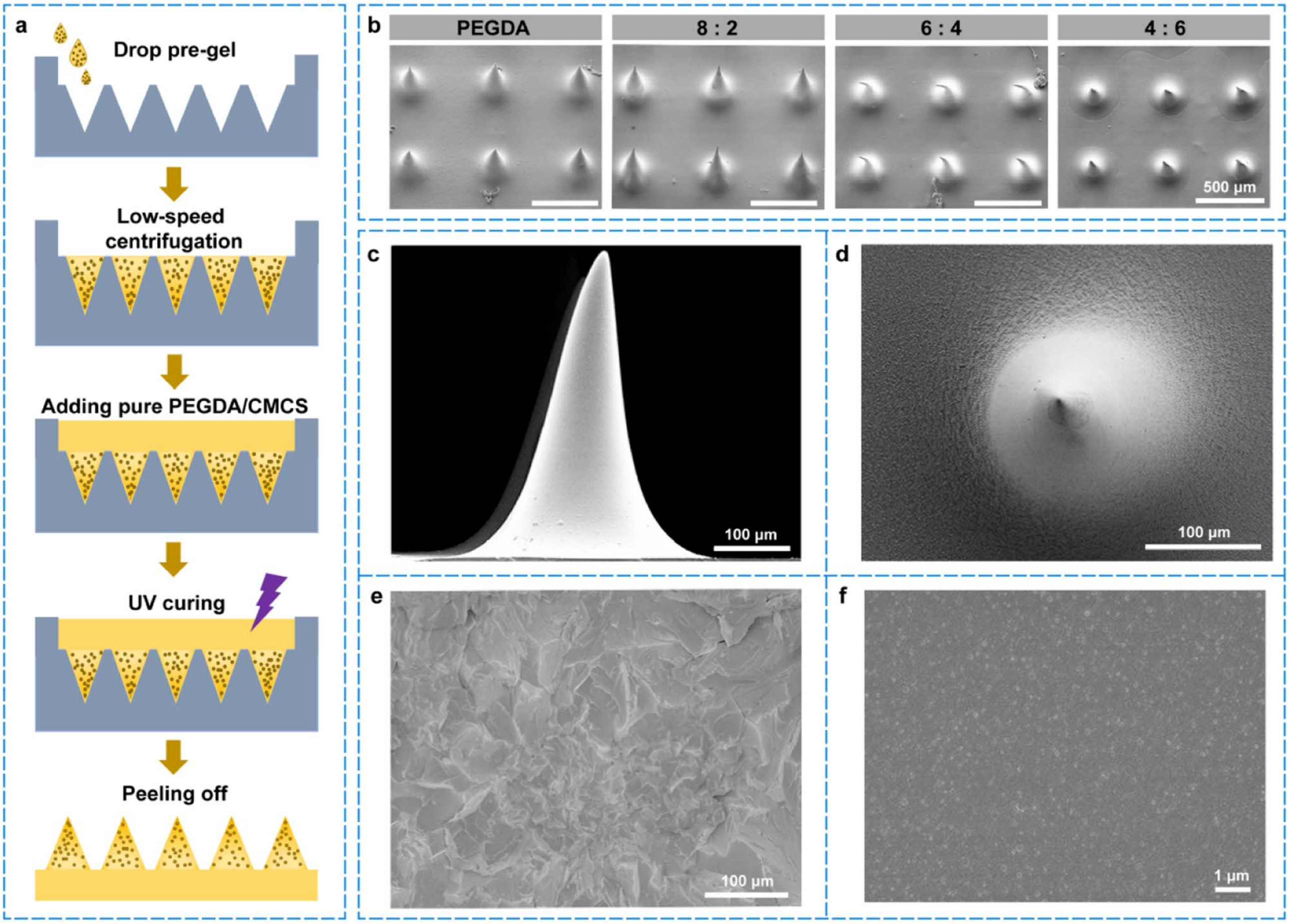

Fig. 2 Characterization of the MNs: (a) SEM image of MNs with different ratios of PEGDA/CMCS (pure PEGDA, PEGDA/CMCS = 8 : 2, 6 : 4, and 4 : 6); (b) schematic diagram of the MN fabrication process; (c and d) SEM images showing the side view and the vertical view of the microneedle tip; (e) SEM images showing the microporous surface structure of the Cu@ZIF-8 loaded MNs; (f) SEM images showing Cu@ZIF-8 nanoparticles encapsulated in the MNs; scale bars are 500 μm in (a), 100 μm in (c)–(e), and 1 μm in (f).

easy collapse of the needle bodies. As shown in Fig. 2c and d, the MNs (PEGDA/CMCS = 8 : 2) display a complete complementary conical structure of the negative mold. The MNs' height and base diameter were 410 μm and 200 μm, respectively. The MNs prepared using the ratio of 8 : 2 exhibited a porous structure after lyophilization, as shown in the scanning electron microscope (SEM) images (Fig. 2e), which is conducive to the diffusion of Cu@ZIF-8 nanoparticles and the contact between bacteria and materials. It is worth noting that the SEM images also demonstrated that the Cu@ZIF-8 nanoparticles were uniformly distributed inside the needle body, indicating favorable loading performance (Fig. 2f). We also conducted an energy-dispersive X-ray spectroscopy (EDS) mapping to further explore the element composition of MNs (Fig. S2†). In the images, the red dots were related to the Cu element, the pink dots were related to the Zn element, the blue dots were related to the C element, and the green dots were related to the O element, respectively. Almost no Cu and Zn elements were present in the images of MNs without Cu@ZIF-8 loaded, whereas there was obviously the existence of Cu and Zn elements in Cu@ZIF-8 loaded MNs, and the element density increased with the increased concentration of Cu@ZIF-8. All these results confirmed the successful preparation of Cu@ZIF-8 loaded MNs.

The CMCS substrate makes microneedles have good biodegradability as well as good antibacterial properties and the addition of PEGDA enhances the mechanical properties of microneedles. We evaluated the impact of the PEGDA content on the properties of hydrogels to determine the optimal mechanical strength and degradation ability of hydrogels for MN preparation. Notably, the compressive strength of MNs crucially depends on the concentration of PEGDA and the addition of PEGDA amplified the strength of hydrogels. Mechanical compression tests were performed using a testing machine to compare the mechanical properties of these four microneedles of different proportions. With the increase in the compression displacement (Fig. S3†), the force between the probe and the microneedles increased continuously. Microneedles with a higher ratio of PEGDA exhibited higher mechanical strength. These results indicated that the ratio of PEGDA : CMCS may be a crucial parameter in influencing the mechanical properties of microneedles. Meanwhile, the Young's modulus of the hydrogel MNs increased remarkably with a higher ratio of PEGDA/CMCS. The PEGDA/CMCS = 8 : 2 groups exhibited good mechanical strength similar to that of pure PEGDA-MNs (Fig. 3a), which proved to be more suitable for the manufacture of porous MN patches that required good mechanical strength.

According to previous research, insertion force into skin for microneedles with a tip radius of 30 to 80 μm, ranged from 0.08 N to 3 N, and the average insertion force for hollow microneedles is 1.65 ± 0.03 N while the insertion force for solid microneedles is 1.29 ± 0.04 N.[39] From the results obtained in the compression test for our microneedles (Fig. S3†), the mechanical properties of the PEGDA : CMCS = 8 : 2 group are good enough to pierce skin, which can be visually demonstrated in the subsequent puncture pathological staining(Fig. 3d).

Besides, *in vitro* degradation behavior of the MNs in PBS solution at 37 °C was investigated within two weeks. The degradation rate was faster during the first week; later, the

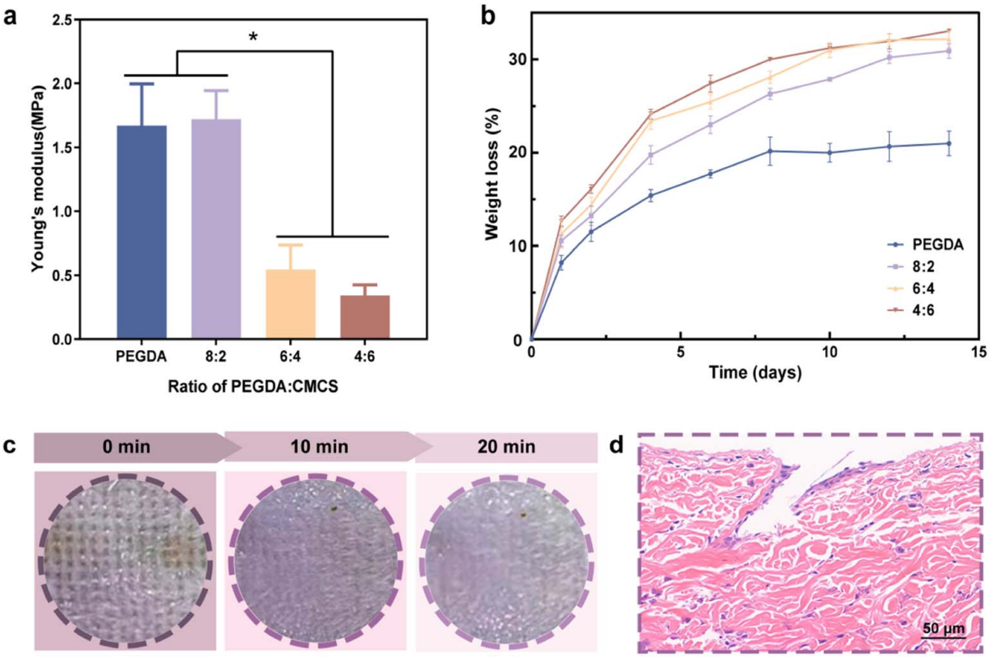

Fig. 3 (a) Young's modulus of MNs with different ratios of PEGDA/CMCS; (b) *In vitro* degradation behavior of the MNs with different ratios of PEGDA/CMCS; (c) optical images of hair-removed rat dorsal skin after insertion, and skin recovery after the removal of the MNs. (d) H&E stained cross-section of skin with MNs inserted; scale bars are 50 μm in (d). Data are shown as mean ± SD ($n = 3$) and analyzed using the one-way ANOVA test.

degradation slowed. However, the degradation rate increased with the addition of CMCS. It is worth noting that the PEGDA/CMCS = 8 : 2 MNs exhibited excellent mechanical strength as well as good degradation ability, which is beneficial to the puncture of skin and the diffusion of Cu@ZIF-8. The PEGDA/CMCS MNs had a degradation rate close to 30% after 2 weeks, while the degradation rate was no more than 20% for pure PEGDA MNs (Fig. 3b).

To intuitively present the application effect of MNs, we applied an MN patch (PEGDA/CMCS = 8 : 2) to the dorsal skin of rats. After MN puncturing of the rat's subcutaneous tissue, obvious indentations were observed. As shown in Fig. 3c, the puncture marks gradually disappeared, and the skin almost returned to its normal state within 20 min of removing the MNs from the skin. Moreover, there was no obvious irritative reaction (*e.g.*, swelling and erythema) on the skin, indicating that the MN is a minimally invasive approach for achieving drug delivery.[40] The histology of the puncture site further confirmed that MNs successfully penetrated the epidermis to a depth of approximately 200 μm, as shown in the HE images (Fig. 3d). Notably, the insertion depth in the skin was less than the original height of the MNs (∼410 μm), mainly owing to the compressive deformation of the MNs in the skin and the viscoelastic properties of natural skin. Compared with conventional dressings, such PEGDA/CMCS-MN arrays were able to deliver drugs into severe wounds attached to blood clots and adipose tissue more effectively because of their high specific surface area as well as puncture ability. Thus, MNs fabricated by using PEGDA/CMCS at a ratio of 8 : 2 were adopted to effectively exert their drug delivery and repair effects, benefiting from the optimized degradation rate and good mechanical strength.

3.3. The antibacterial properties of PCCZMNs

Wounds exposed to the external environment are vulnerable to infection by malignant bacteria, such as *S. aureus*, which may cause sepsis and even life-threatening complications. Thus, prevention of bacterial infection is key in the wound healing process. To detect the concentration of ROS dispersed in the incubation solution, the absorbance of the bacterial supernatant was used as an index of the ROS concentration using the hydroxylamine colorimetric method (Fig. 4a). We found that the color depth of 1.5 mg mL^{-1} Cu@ZIF-8 nanoparticles was darker compared with that of 1.5 mg mL^{-1} ZIF-8 nanoparticles, indicating that Cu@ZIF-8 nanoparticles tend to generate a higher concentration of ROS that kill bacteria more efficiently. Meanwhile, the concentration of ROS in the supernatant was detected using a ROS detection kit (Fig. 4b), which revealed that compared with the ZIF-8 nanoparticles, the Cu@ZIF-8 nanoparticles generated more reactive oxygen species, which contributed to their antibacterial properties.[41,42] The concentration of copper ions and zinc ions released from MNs was analyzed by using an enzyme labeler. The release curve revealed that the ions that were slowly and continuously released from the MNs positively correlated with the gradual degradation of the MNs, showing a steady upward trend within a week (Fig. 4c and S4†). To further verify the antibacterial activity of the PCCZMNs *in vitro*, MNs with different Cu@ZIF-8 concentrations ranging from 0 to 2.5 mg mL^{-1} (PCMN, PCCZMN-L, PCCZMN-M, and PCCZMN-H) were co-cultured with *E. coli* and *S. aureus*. The plate-counting method was then applied to the strains of *S. aureus* and *E. coli*. The number of bacterial colonies in the Cu@ZIF-8 loaded groups (PCCZMNs) was fewer than that in the PCMNs and control groups, while the number of bacterial colonies in the PCMN groups was lower than that in the control group. Fig. 4d–f show that the antibacterial activity was proportional to the concentration of Cu@ZIF-8 nanoparticles, indicating that a higher concentration of Cu@ZIF-8 tended to kill bacteria more efficiently, whereas PCMNs had slight antibacterial activity because of the antibacterial effect of CMCS. This result confirmed the assumption that the PEGDA/CMCS scaffold possessed antibacterial activity. More importantly, the addition of Cu@ZIF-8 substantially improved the antibacterial activity of MNs, which is essential to accelerate wound healing. From the above experiments, we conclude that PCCZMNs have outstanding potential for antibacterial action.

3.4. Biocompatibility of PCCZMNs

To investigate the most appropriate concentration of Cu@ZIF-8 nanoparticles, we utilized the leaching solution originating from MNs to co-culture three different cells, which plays an important part in wound healing, and cell viability was detected by using the CCK-8 assay. As displayed in Fig. 5a, when co-cultured with HUVECs, the OD value at 450 nm tested by using the CCK-8 assay revealed that all groups showed time-dependent proliferation rates. More importantly, once the concentration of Cu@ZIF-8 nanoparticles exceeded 1.5 mg mL^{-1} (PCCZMN-M), the proportion of living cells decreased significantly, indicating an obvious suppression effect against cell growth. The corresponding normalized cell viability (Fig. 5b) showed similar results. In the biocompatibility tests of L929 fibroblasts and macrophages, we observed that the high concentration of Cu@ZIF-8 nanoparticles (PCCZMN-H) is toxic to both types of cells (Fig. S5†). Combining the results of the antibacterial experiments, Cu@ZIF-8 nanoparticles with a concentration of 1.5 mg mL^{-1} were advisable to fabricate MNs that simultaneously possessed acceptable cell biocompatibility and excellent antibacterial effectiveness.

3.5. Angiogenesis properties of PEGDA/CMCS-Cu@ZIF-8-MN

Newly formed vessels can deliver nutrition and oxygen to the wounds to accelerate wound closure.[34,43] Therefore, HUVEC migration and tube formation are essential steps during angiogenesis that determine the curative effect of wound healing. PCCZMNs encapsulated with Cu@ZIF-8 (1.5 mg ml^{-1}) were used in the angiogenic test. As shown in Fig. 6a and b, PCCZMNs showed higher efficiency than PCMNs in promoting HUVEC tube formation, characterized by more visible tube-like structures and a higher tube length. Meanwhile, PCCZMNs showed a higher migration rate (79.76 ± 1.24%) than PCMNs (45.38 ± 0.47%) at an interval of 24 h (Fig. 6c and d). This suggests that the PCCZMNs with a concentration of 1.5 mg ml^{-1}

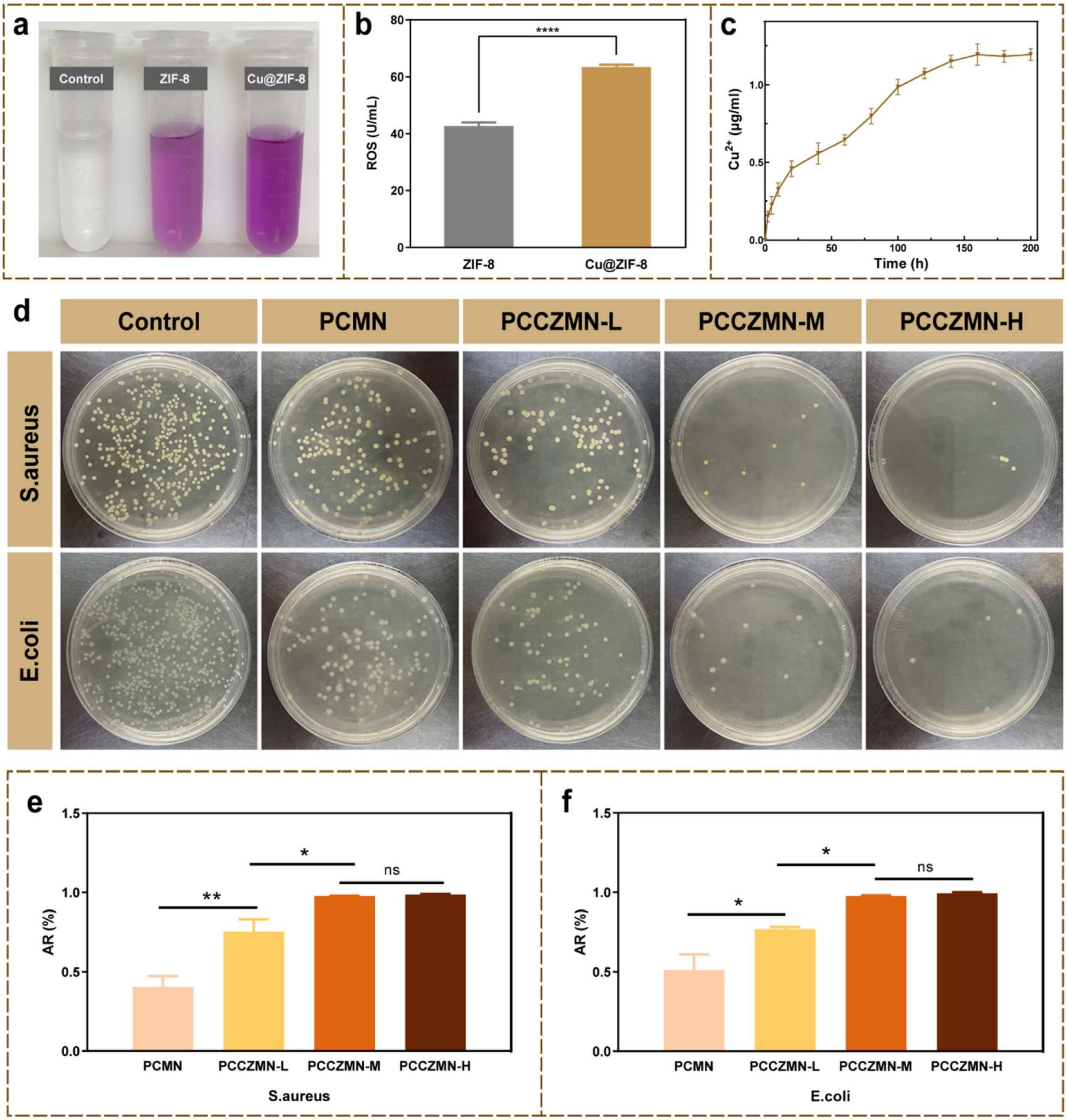

Fig. 4 Cu@ZIF-8 nanoparticle characterization and antibacterial properties: (a) the color change of Cu@ZIF-8 and ZIF-8 nanoparticles. (b) Graph of the ROS generation assay with Cu@ZIF-8 and ZIF-8 nanoparticles. (c) The release curve of Cu ions decomposed from MNs; the concentration of Cu@ZIF-8 and ZIF-8 nanoparticles in MNs is 1.5 mg mL^{-1}. (d) The representative colony forming unit images and (e and f) corresponding quantitative analysis of *S. aureus* and *E. coli*; data are shown as mean ± SD ($n = 3$) and analyzed using the one-way ANOVA test.

Cu@ZIF-8 exhibit an angiogenesis inducing effect, which was attributed to the Cu ion release. A well-established vascular network can effectively promote the delivery of nutrients, thereby enhancing wound repair. Combined with the results of HUVEC migration and *in vitro* tube formation experiments, PCCZMNs showed the best angiogenic activity and were used for subsequent *in vivo* experiments.

3.6. Evaluation of the MNs for wound healing

To further investigate the practical value of PCCZMNs for wound healing, we established a full-thickness cutaneous defect rat model by creating 1 cm round wounds on their backs. The rats were randomly divided into three groups: control, PCMN and PCCZMN. In the wound healing process, the changes in the wound bed were photographed and measured on

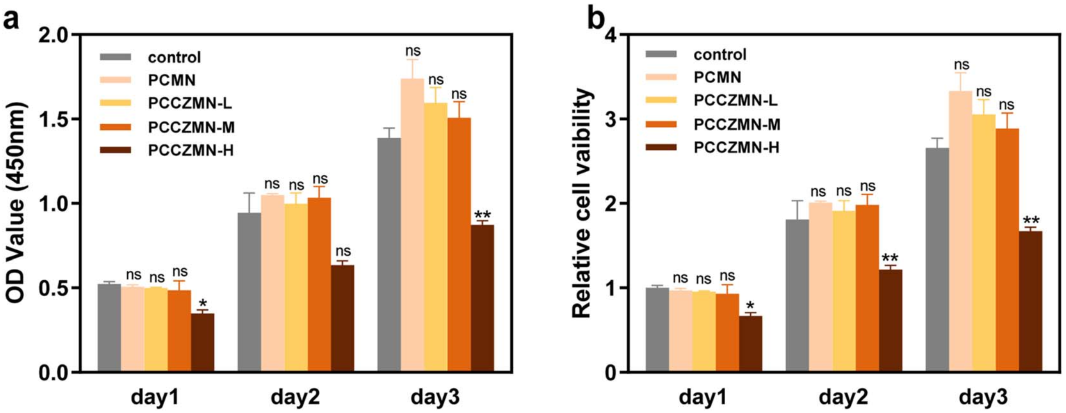

Fig. 5 (a and b) The OD value and the corresponding cell viability of MNs with different Cu@ZIF-8 concentrations evaluated by the CCK-8 test. Data are shown as mean ± SD ($n = 3$) and analyzed using the one-way ANOVA test.

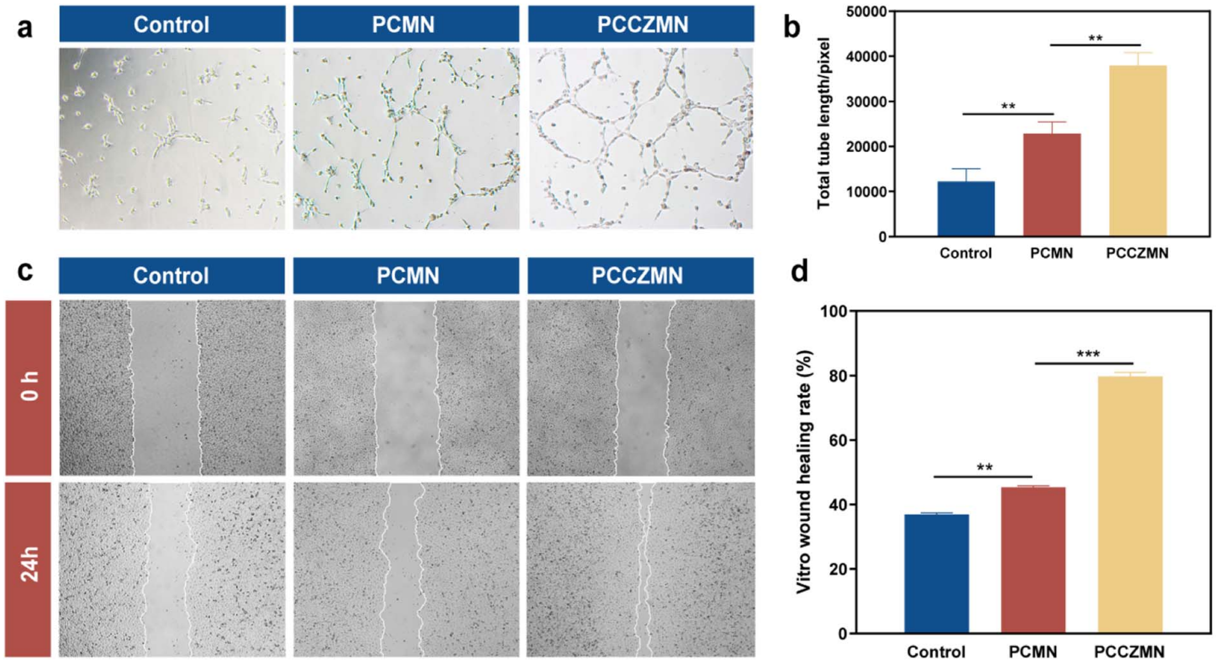

Fig. 6 *In vitro* angiogenic and migration assays: (a) brightfield images of HUVECs incubated on solidified Matrigel substrates in a normal cell culture medium (control) or cultured in a MN extract for 6 h; (b) quantification of the tube length in each group; (c) brightfield images of migrated HUVECs cultured in a normal cell culture medium (control) or cultured in a MN extract for 24 h. (d) Quantification of migrated HUVECs at 24 h. The concentration of Cu@ZIF-8 in PCCZ-MN is 1.5 mg ml^{-1}.

the 0, 4th, 8th, and 16th days, as shown in Fig. 7a. Generally, the round wounds on the backs of the rats were nearly healed after 16 days in the PCCZMN group with a Cu@ZIF-8 concentration of 1.5 mg mL^{-1}, while the wounds showed a slower healing rate in the PCMN and control groups (Fig. 7a and b). The ability of Cu@ZIF-8 encapsulated MNs to promote wound healing *in vivo* was due to the great antimicrobial capacity, as well as the significant angiogenic effect during the period of degradation, which could be proven in the PCCZMN group. The body temperatures of the rats were measured at various time points. As shown in Fig. 7c, the mean body temperature of the PCCZMN group was relatively lower than that of the other groups, especially the control group, and the relatively lower body temperature reflected a less severe inflammatory condition.

The degree of re-epithelialization is always considered a suitable evaluation standard for wound renovation. To investigate the reconstruction of epidermal tissue, histological tests were performed on the 8th and 16th days of the *in vivo* experiment. Hematoxylin and eosin (H&E) and Masson's trichrome staining, as shown in Fig. 8a–c, indicated that the control group exhibited a maximum wound length of 6.792 ± 0.204 mm on the 8th day and 5.297 ± 0.248 mm on the 16th day. The results for the PCMN groups were 5.683 ± 0.393 mm on the 8th day and 3.859 ± 0.095 mm on the 16th day, indicating

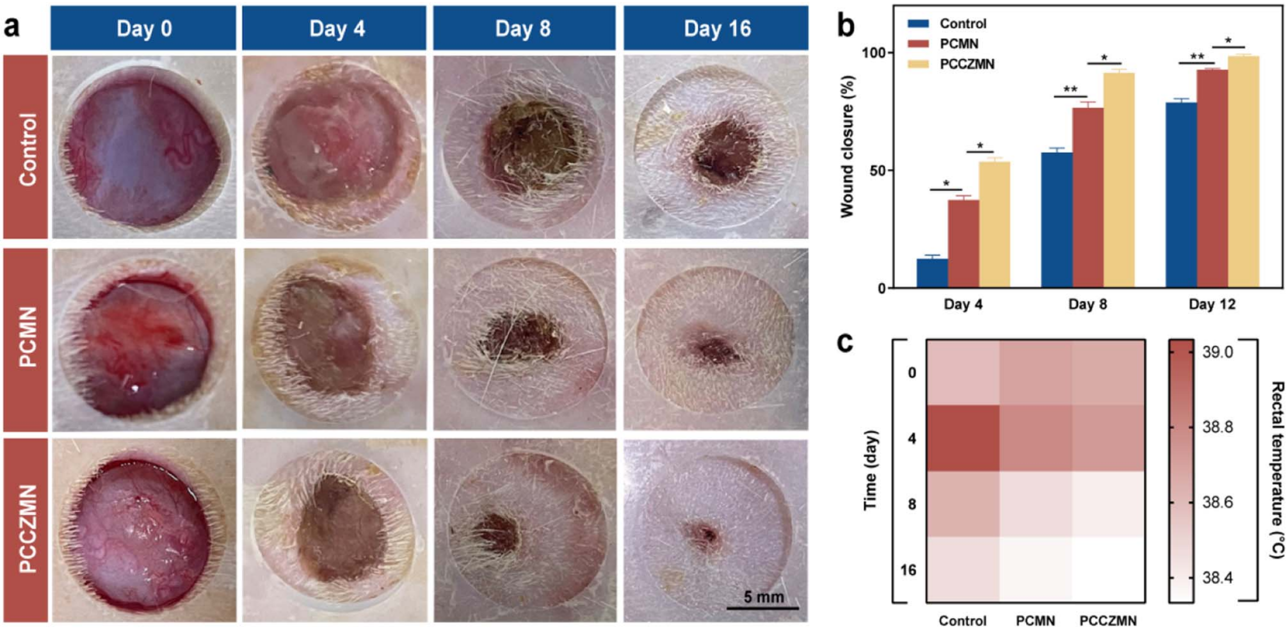

Fig. 7 Evaluation of the MNs for wound healing: (a) optical photograph of the skin wounds in different groups (control, PCMNs, PCCZMNs) within 16 days; (b) quantitative analysis of the wound area compared in three groups; (c) the body temperature of rats at various time points.

a medium healing level. The PCCZMN group exhibited minimal wound length, reaching 3.552 ± 0.364 mm on the 8th day and 1.159 ± 0.271 mm on the 16th day. From the magnification images of H&E staining and Masson's trichrome staining (Fig. 8 and S6†), the PCCZMN group showed the thickest and most complete stratum corneum, indicating the excellent healing effect of Cu@ZIF-8. Furthermore, many hair follicles were visible in the PCCZMN group, indicating that it can promote tissue regeneration compared with other groups. Meanwhile, because of the prominent repairability of the PEGDA/CMCS hydrogel, wounds treated with PCMNs presented better stratum corneum conditions than the control group. As shown in ESI Fig. S2,† the most abundant collagen deposition appeared in the group treated with PCCZMNs containing 1.5 mg mL^{-1} Cu@ZIF-8 nanoparticles, showing prominent deep blue and neatly arranged collagen networks, much higher than those in the PCMN group. In addition, collagen deposition was relatively dense in the PCMN group compared with the control group, indicating the positive matrix reconstruction effect caused by PEGDA/CMCS hydrogel decomposition. These results demonstrated that PCCZMN has the ability to accelerate wound closure, collagen formation, and re-epithelialization.

Neovascularization can reflect the degree of tissue reconstruction and restoration of skin function. Immunofluorescent staining of CD31, a common marker of endothelial cells, was used to analyze neovascularization at wound sites. As shown in Fig. 8d and e, a low density of cell markers was observed in the control group, suggesting a low level of vascularization. In contrast, the blood vessel area in the other groups significantly increased, especially in the PCCZMN group (Fig. 8d and e). This difference was ascribed to Cu@ZIF-8 as well as the microstructure of the needle body fabricated by the PEGDA/CMCS hydrogel, which provided a larger specific surface area for interaction with the wound area, which was beneficial for nutrient exchange and endothelial cell migration.

Inflammation can hinder wound healing in the wound bed. M2 macrophages are essential for wound healing, as they can secrete high amounts of IL-10 and TGF-β to suppress inflammation and contribute to tissue repair, remodeling, vascularization, and retention of homeostasis.[34] It has been established that CD206 is classified into the marker of an alternatively activated M2 phenotype and acts as a hemoglobin scavenger receptor on a macrophage.[35] The wound repair condition was reflected by counting the number of M2 macrophages through immunohistochemical staining of CD206. As shown in Fig. S7,† M2 macrophages stained positively to various degrees in all the groups. In particular, the density of PCCZMNs in the wound beds was the highest among all the groups. In addition, we found that CD206 M2-like cells were outnumbered in the PCMN groups compared with the control groups. This phenomenon indicated that a moderate dose of Cu@ZIF-8 displayed outstanding performance in reducing inflammation at the wound bed, which was not only helpful in killing the microbes, but also promoted the regeneration of neonatal epithelium tissues. Thus, all the histological results proved that the PCCZMNs were conducive to epithelial regeneration and neovascularization, and had an anti-inflammatory effect to a great extent, offering a promising approach for wound healing and other clinical applications. In future research, we will further optimize the design of our microneedles such as enhance the adhesion capability of our microneedles and apply the microneedles to the treatment of diabetic wound models and infection wound models. We believe that after improving material design and applying newly designed MNs to the treatment of a chronic wound model, our future research will offer a promising approach for wound healing and other clinical applications, and benefit clinical patients to a greater extent.

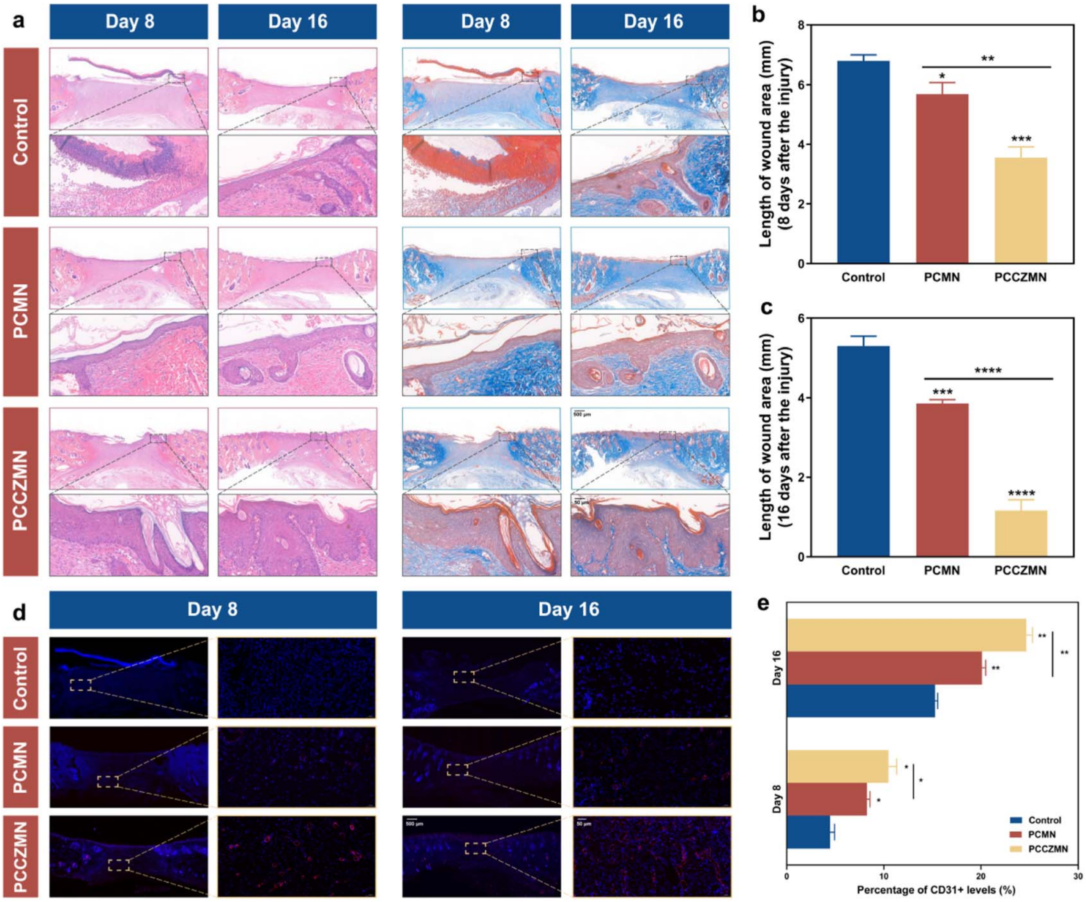

Fig. 8 (a) HE staining and Masson's trichrome staining of the wounds in different treatment groups: the control group, PCMN group and PCCZMN group on the 8th day and 16th day. (b and c) Corresponding quantitative analysis of wound length in different treatment groups. (d) Immunofluorescence staining of CD31 of granulation tissues in different groups on the 8th day and 16th day. (e) Corresponding quantitative analysis of CD31 micro-vessel density in different treatment groups.

4 Conclusion

In this study, we developed PEGDA/CMCS MNs loaded with Cu@ZIF-8 nanoparticles for the treatment of full-thickness cutaneous defects. The MNs exhibited good biocompatibility and mechanical properties, and were able to deliver active ingredients into wounds more effectively because of their high specific surface area and puncture ability. The MNs were a minimally invasive approach because of the small size of the needles. More importantly, the MNs showed excellent antibacterial and angiogenic properties, significantly promoted re-epithelialization, angiogenesis, and collagen deposition, and reduced inflammation in wounds. In conclusion, our study utilized Cu@ZIF-8 nanoparticle-encapsulated PEGDA/CMCS-MNs, which demonstrated good potential for wound healing.

Author contributions

JX and YZ conceived and designed the experiments, performed the experiments, analyzed the data, prepared the figures and approved the final draft. YX analyzed the data and prepared the figures. JX, YZ and HC performed the animal experiments. LZ and DC helped perform the analysis with constructive discussions. JG reviewed the drafts of the manuscript. LG, LC and MW conceived and designed the experiments, reviewed drafts of the manuscript, provided financial support, and approved the final draft.

Ethical statement

The animal study was reviewed and approved by the Experimental Animal Welfare Ethics Committee, Zhongnan Hospital of Wuhan University.

Conflicts of interest

The authors declare that the research was conducted in the absence of any commercial or financial relationships that could be construed as a potential conflict of interest.

Acknowledgements

This work was supported by the Scientific Research Project of the Health Commission of Hubei Province (WJ2021M159) and

Zhongnan Hospital Science and Technology Innovation Cultivation Foundation (CXPY2020039). We would like to thank each of the authors for their contribution to this study.

References

1 T. Sheng, B. Luo, W. Zhang, *et al.*, Microneedle-Mediated Vaccination: Innovation and Translation, *Adv. Drug Delivery Rev.*, 2021, **179**, 113919.

2 C. Wang, Y. Ye, G. M. Hochu, *et al.*, Enhanced Cancer Immunotherapy by Microneedle Patch-Assisted Delivery of Anti-PD1 Antibody, *Nano Lett.*, 2016, **16**(4), 2334–2340.

3 A. Ghavaminejad, J. Li, B. Lu, *et al.*, Glucose-Responsive Composite Microneedle Patch for Hypoglycemia-Triggered Delivery of Native Glucagon, *Adv. Mater.*, 2019, **31**(30), e1901051.

4 K. Lee, Y. Xue, J. Lee, *et al.*, A Patch of Detachable Hybrid Microneedle Depot for Localized Delivery of Mesenchymal Stem Cells in Regeneration Therapy, *Adv. Funct. Mater.*, 2020, **30**(23), 2000086.

5 X. Zhou, X. Jiang, M. Qu, *et al.*, Engineering Antiviral Vaccines, *ACS Nano*, 2020, **14**(10), 12370–12389.

6 X. Zhang, G. Chen, Y. Yu, *et al.*, Bioinspired Adhesive and Antibacterial Microneedles for Versatile Transdermal Drug Delivery, *Research*, 2020, **2020**, 3672120.

7 G. S. Liu, Y. Kong, Y. Wang, *et al.*, Microneedles for transdermal diagnostics: Recent advances and new horizons, *Biomaterials*, 2020, **232**, 119740.

8 M. L. W. Juhasz and J. L. Cohen, Microneedling for the Treatment of Scars: An Update for Clinicians, *Clin. Cosmet. Investig. Dermatol.*, 2020, **13**, 997–1003.

9 Y. Su, V. L. Mainardi, H. Wang, *et al.*, Dissolvable Microneedles Coupled with Nanofiber Dressings Eradicate Biofilms via Effectively Delivering a Database-Designed Antimicrobial Peptide, *ACS Nano*, 2020, **14**(9), 11775–11786.

10 E. Y. Jeon, J. Lee, B. J. Kim, *et al.*, Bio-inspired swellable hydrogel-forming double-layered adhesive microneedle protein patch for regenerative internal/external surgical closure, *Biomaterials*, 2019, **222**, 119439.

11 J. Chi, X. Zhang, C. Chen, *et al.*, Antibacterial and angiogenic chitosan microneedle array patch for promoting wound healing, *Bioact. Mater.*, 2020, **5**(2), 253–259.

12 X. Zhang, G. Chen, Y. Liu, *et al.*, Black Phosphorus-Loaded Separable Microneedles as Responsive Oxygen Delivery Carriers for Wound Healing, *ACS Nano*, 2020, **14**(5), 5901–5908.

13 W. He, Z. Wang, C. Hou, *et al.*, Mucus-Inspired Supramolecular Adhesives with Oil-Regulated Molecular Configurations and Long-Lasting Antibacterial Properties, *ACS Appl. Mater. Interfaces*, 2020, **12**(14), 16877–16886.

14 M. Kalaj and S. M. Cohen, Postsynthetic Modification: An Enabling Technology for the Advancement of Metal-Organic Frameworks, *ACS Cent. Sci.*, 2020, **6**(7), 1046–1057.

15 L. Shi, X. Liu, W. Wang, *et al.*, A Self-Pumping Dressing for Draining Excessive Biofluid around Wounds, *Adv. Mater.*, 2019, **31**(5), e1804187.

16 X. Zhang, J. Wang, H. Jin, *et al.*, Bioinspired Supramolecular Lubricating Hydrogel Induced by Shear Force, *J. Am. Chem. Soc.*, 2018, **140**(9), 3186–3189.

17 K. Zhang, Z. Jia, B. Yang, *et al.*, Adaptable Hydrogels Mediate Cofactor-Assisted Activation of Biomarker-Responsive Drug Delivery via Positive Feedback for Enhanced Tissue Regeneration, *Adv. Sci.*, 2018, **5**(12), 1800875.

18 Y. S. Zhang and A. Khademhosseini, Advances in engineering hydrogels, *Science*, 2017, **356**(6337), eaaf3627.

19 W. Zhu, C. Chu, S. Kuddannaya, *et al.*, Vivo Imaging of Composite Hydrogel Scaffold Degradation Using CEST MRI and Two-Color NIR Imaging, *Adv. Funct. Mater.*, 2019, **29**(36), 1903753.

20 X. Su, T. Wang and S. Guo, Applications of 3D printed bone tissue engineering scaffolds in the stem cell field, *Regen. Ther.*, 2021, **16**, 63–72.

21 G. Musumeci, C. Loreto, S. Castorina, *et al.*, New perspectives in the treatment of cartilage damage. Poly(ethylene glycol) diacrylate (PEGDA) scaffold. A review, *Ital. J. Anat Embryol.*, 2013, **118**(2), 204–210.

22 K. Yue, G. Trujillo-De Santiago, M. M. Alvarez, *et al.*, Synthesis, properties, and biomedical applications of gelatin methacryloyl (GelMA) hydrogels, *Biomaterials*, 2015, **73**, 254–271.

23 M. C. G. Pellá, M. K. Lima-Tenório, E. T. Tenório-Neto, *et al.*, Chitosan-based hydrogels: From preparation to biomedical applications, *Carbohydr. Polym.*, 2018, **196**, 233–245.

24 C. Sandoval, G. Ríos, N. Sepúlveda, *et al.*, Effectiveness of Copper Nanoparticles in Wound Healing Process Using In Vivo and In Vitro Studies: A Systematic Review, *Pharmaceutics*, 2022, **14**(9), 1838.

25 J. Salvo and C. Sandoval, Role of copper nanoparticles in wound healing for chronic wounds: literature review, *Burns Trauma*, 2022, **10**, tkab047.

26 Z. Liu, X. Chen and C. Li, Fabrication of a bionic asymmetric wettable Cu-doped chitosan-laponite-PCL wound dressing with rapid healing and antibacterial effect, *Biomed. Mater.*, 2022, **17**(5), 055008.

27 Y. Zhang, M. Chang, F. Bao, *et al.*, Multifunctional Zn doped hollow mesoporous silica/polycaprolactone electrospun membranes with enhanced hair follicle regeneration and antibacterial activity for wound healing, *Nanoscale*, 2019, **11**(13), 6315–6333.

28 H. Xie, H. Xia, L. Huang, *et al.*, Biocompatible, antibacterial and anti-inflammatory zinc ion cross-linked quaternized cellulose-sodium alginate composite sponges for accelerated wound healing, *Int. J. Biol. Macromol.*, 2021, **191**, 27–39.

29 B. Xu, Y. Li, F. Gao, *et al.*, High Strength Multifunctional Multiwalled Hydrogel Tubes: Ion-Triggered Shape Memory, Antibacterial, and Anti-inflammatory Efficacies, *ACS Appl. Mater. Interfaces*, 2015, **7**(30), 16865–16872.

30 F. Zou, J. Jiang, F. Lv, *et al.*, Preparation of antibacterial and osteoconductive 3D-printed PLGA/Cu(I)@ZIF-8 nanocomposite scaffolds for infected bone repair, *J. Nanobiotechnol.*, 2020, **18**(1), 39.

31 S. Yao, J. Chi, Y. Wang, *et al.*, Zn-MOF Encapsulated Antibacterial and Degradable Microneedles Array for Promoting Wound Healing, *Adv. Healthc. Mater.*, 2021, **10**(12), e2100056.

32 A. Kumar, A. Sharma, Y. Chen, *et al.*, Copper@ZIF-8 Core-Shell Nanowires for Reusable Antimicrobial Face Masks, *Adv. Funct. Mater.*, 2021, **31**(10), 2008054.

33 Z. Lin, Y. Cao, J. Zou, *et al.*, Improved osteogenesis and angiogenesis of a novel copper ions doped calcium phosphate cement, *Mater. Sci. Eng., C*, 2020, **114**, 111032.

34 L. M. Cucci, C. Satriano, T. Marzo, *et al.*, Angiogenin and Copper Crossing in Wound Healing, *Int. J. Mol. Sci.*, 2021, **22**(19), 10704.

35 H. Zhang, Q. Zhang, Z. Guo, *et al.*, Disulfiram-loaded metal organic framework for precision cancer treatment via ultrasensitive tumor microenvironment-responsive copper chelation and radical generation, *J. Colloid Interface Sci.*, 2022, **615**, 517–526.

36 C. Liu, D. Wang, S. Zhang, *et al.*, Biodegradable Biomimic Copper/Manganese Silicate Nanospheres for Chemodynamic/Photodynamic Synergistic Therapy with Simultaneous Glutathione Depletion and Hypoxia Relief, *ACS Nano*, 2019, **13**(4), 4267–4277.

37 K. J. Koski, J. J. Cha, B. W. Reed, *et al.*, High-density chemical intercalation of zero-valent copper into Bi2Se3 nanoribbons, *J. Am. Chem. Soc.*, 2012, **134**(18), 7584–7587.

38 Y. Dai, P. Xing, X. Cui, *et al.*, Coexistence of Cu(ii) and Cu(i) in Cu ion-doped zeolitic imidazolate frameworks (ZIF-8) for the dehydrogenative coupling of silanes with alcohols, *Dalton Trans.*, 2019, **48**(44), 16562–16568.

39 S. P. Davis, B. J. Landis, Z. H. Adams, *et al.*, Insertion of microneedles into skin: measurement and prediction of insertion force and needle fracture force, *J. Biomech.*, 2004, **37**(8), 1155–1163.

40 P. Liu, H. Du, Z. Wu, *et al.*, Hydrophilic and anti-adhesive modification of porous polymer microneedles for rapid dermal interstitial fluid extraction, *J. Mater. Chem. B*, 2021, **9**(27), 5476–5483.

41 H. Lee, H. J. Lee, J. Seo, *et al.*, Activation of Oxygen and Hydrogen Peroxide by Copper(II) Coupled with Hydroxylamine for Oxidation of Organic Contaminants, *Environ. Sci. Technol.*, 2016, **50**(15), 8231–8238.

42 S. Zhao, D. Miao, K. Zhu, *et al.*, Interaction of benzo[a]pyrene with Cu(II)-montmorillonite: generation and toxicity of environmentally persistent free radicals and reactive oxygen species, *Environ. Int.*, 2019, **129**, 154–163.

43 W. Ma, X. Zhang, Y. Liu, *et al.*, Polydopamine Decorated Microneedles with Fe-MSC-Derived Nanovesicles Encapsulation for Wound Healing, *Adv. Sci.*, 2022, **9**(13), e2103317.